Chem

CellPress

Article

Toward Phase and Catalysis Control: Tracking the Formation of Intermetallic Nanoparticles at Atomic Scale

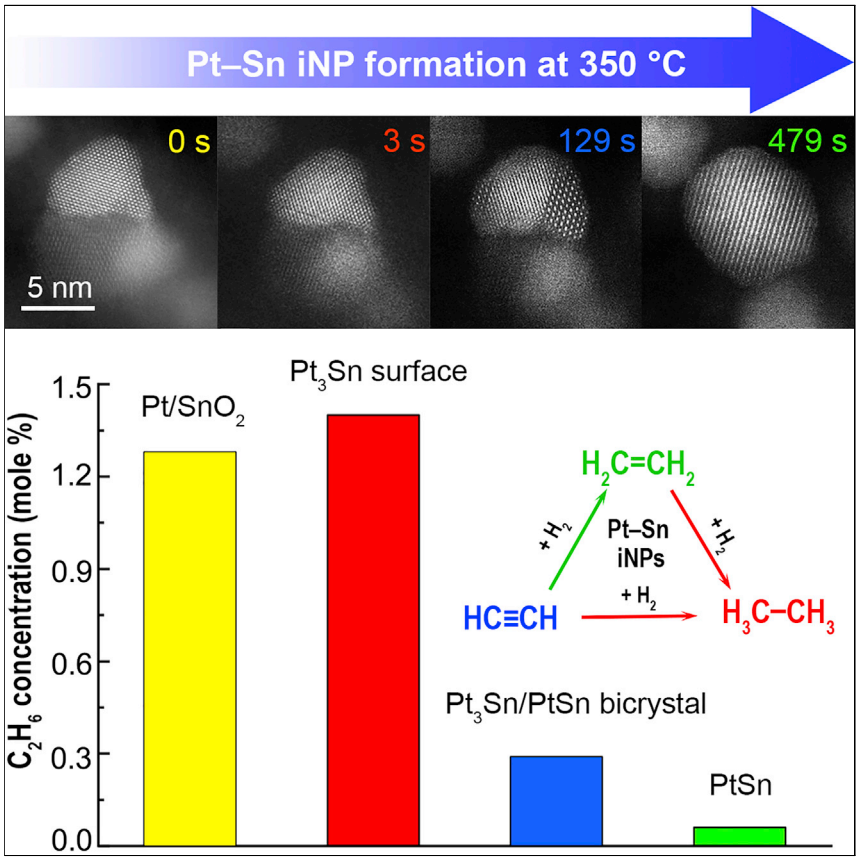

We have monitored the formation process of Pt-Sn intermetallic nanoparticles at atomic scale by using *in situ* aberration-corrected transmission electron microscopy. This provides direct imaging of the alloying mechanism in bimetallic nanoscale systems. The surface-mediated Sn diffusion and a coherent Pt_3Sn/PtSn interface are responsible for overall reaction dynamics. These new insights allowed us to control the phases of these Pt-Sn iNPs and thereby tune catalysis of the acetylene semi-hydrogenation reaction.

Tao Ma, Shuai Wang, Minda Chen, ..., Matthew J. Kramer, Wenyu Huang, Lin Zhou

whuang@iastate.edu (W.H.)
linzhou@ameslab.gov (L.Z.)

HIGHLIGHTS

Consecutive formation of Pt_3Sn and PtSn was observed in real time at atomic scale

The surface-mediated Sn diffusion is key to controlling overall reaction dynamics

A coherent Pt_3Sn/PtSn interface lowers activation energy of phase transformation

Controlled phase selection was achieved, resulting in tunable catalytic performance

Ma et al., Chem 5, 1235–1247
May 9, 2019
https://doi.org/10.1016/j.chempr.2019.02.026

Chem

CellPress

Article

Toward Phase and Catalysis Control: Tracking the Formation of Intermetallic Nanoparticles at Atomic Scale

Tao Ma,[1] Shuai Wang,[2] Minda Chen,[3] Raghu V. Maligal-Ganesh,[3] Lin-Lin Wang,[1] Duane D. Johnson,[1,4] Matthew J. Kramer,[1,4] Wenyu Huang,[3,*] and Lin Zhou[1,4,5,*]

SUMMARY

Intermetallic nanoparticles (iNPs) have yielded enormous successes in catalytic applications by the formation of ordered phases. However, atomic-level understanding of the alloying mechanism, which plays a pivotal role in controlling intermetallic phases and tailoring their catalytic properties, is still elusive. In this study, we discovered a consecutive formation of ordered Pt_3Sn and PtSn phases during the growth of Pt-Sn iNP inside a well-defined nano-reactor at elevated temperature by using *in situ* scanning transmission electron microscopy. We found that the surface-mediated diffusion of Sn controls overall dynamics of the reaction, while the unique coherent interfacial structure is determinative for the PtSn transformation. We then further controlled the phase selection of Pt-Sn iNPs and demonstrated their distinguishable catalytic behaviors. Our findings not only provide detailed experimental evidence on the alloying mechanism in intermetallic nanoscale systems but also pave the way for mechanistic control of synthesis and catalytic properties of iNPs.

INTRODUCTION

Intermetallic compounds have drawn great attention for catalytic applications because of their dramatically improved activity, selectivity, and stability.[1–10] Design and synthesis of intermetallic nanoparticles (iNPs), bearing a high surface-to-volume ratio, are thus highly desired for an increased number of active sites. Being a solid-state mixture of two or more metal components, iNPs possess not only modified crystal structures to accommodate different elements but also altered surface geometric and electronic structures that could directly correlate with catalytic activity and selectivity,[11,12] given that the adsorption of reactive species is highly dependent on the structure of the active sites.[13–15]

Intermetallic structures tend to minimize their free energy by forming atomic configurations commensurate with strong chemical bonds. As a result, different elements can alternate in specific sites and form ordered phases. Such ordering transformations are of great interest because these structures can lead to distinguishable and often controllable electronic,[16] magnetic,[17,18] and chemical[19,20] properties, often predictable from thermodynamics and kinetics considerations.[21,22] For bulk materials, phase diagrams that describe the alloying behaviors of metals have been established in many systems, providing key guidance for the alloy design and development.[23] However, at the nanoscale, the limited dimensions of nanoparticles raise a quantum-size effect that can strongly modify the thermodynamics and kinetic stability of many intermetallic compounds.[24] Indeed, different alloying behaviors are evident between bulk and iNPs.

The Bigger Picture

How do atoms rearrange in a solid-state reaction to form new structures, especially in catalytic systems with dramatic property difference? Understanding atomic dynamics is key to achieving controlled synthesis of catalysts and other materials. Using advanced electron microscopy, we directly monitor the rearrangement of atoms during a reaction between nanocrystalline Pt and SnO_2 and observe consecutive formation of Pt_3Sn and PtSn. This real-time imaging provides invaluable understanding of the alloying mechanisms in intermetallic nanoscale systems, which enables precise phase selection and thereby control of the catalytic properties, as we demonstrate for the semi-hydrogenation of acetylene. In pursuit of fully controlled synthesis of intermetallic nanoparticles, our results have made an important step forward in the structure manipulation to serve society with more efficient and affordable energy and chemistry.

For example, in the bulk Pt-Sn system, obtaining the ordered Pt_3Sn and PtSn requires melting of pure Pt and Sn in the appropriate ratios and then high-temperature treatments such as zone refining.[25,26] In contrast, these phases can be easily formed in the iNPs: Pt_3Sn is obtained, e.g., by annealing the Pt-Sn nanoparticles at 300°C to 600°C[27–30]; PtSn forms at temperatures even below 300°C.[27,29,30] The increased surface area, which facilitates mass transportation via surface diffusion, is believed to reduce the energy barrier of the ordering transformations in iNPs.[31] On the other hand, when ordering occurs, the introduction of phase boundaries increases the system energy, opposing the formation of ordered phases.[32] These two competing effects are generally active in nanoscale systems and can be influenced by the size, shape, and interfacial energies of iNPs. Such complicated pathways deviate iNPs from the well-established bulk phase diagrams, making it more difficult to design and fabricate multifunctional iNPs at the nanoscale.

This study aimed to unravel these competing effects by directly monitoring the formation of ordered phases in iNPs at the atomic level. This was achieved with a silica-confined nano-reactor, in which single reactant pairs of Pt/SnO_2 particles were encapsulated by mesoporous silica shells ($Pt/SnO_2@mSiO_2$). This elaborate structure was synthesized by polymerizing the silica layer around the surface of nanoparticles according to a sol-gel process (see Experimental Procedures for details). The nano-reactor can isolate the reactant pairs up to 750°C without sintering and aggregation,[29,33] providing a stable platform by which we can study chemical diffusion and phase transformations in the reactant pairs at elevated temperature. High-angle annular dark-field scanning transmission electron microscopy (HAADF-STEM), which can simultaneously provide atomic spatial resolution and chemical sensitivity (*Z* contrast),[34–36] was employed to observe the movement of Pt and Sn atoms during the reaction. In addition, the formation of ordered Pt-Sn iNPs requires the reduction of SnO_2, which can be facilitated by the electron beam (as the reducing agent). Therefore, we were able to precisely control and monitor the transformation process using a sub-angstrom electron probe. We discovered that the reaction pathway between Pt and SnO_2 follows a consecutive formation of ordered Pt_3Sn and PtSn. A unique coherent interface, $(110)_{Pt_3Sn} \parallel (001)_{PtSn}$ and $[1\bar{1}0]_{Pt_3Sn} \parallel [210]_{PtSn}$, was observed during the $Pt_3Sn \rightarrow PtSn$ transformation. Combining *in situ* atomic-scale observations and theoretical calculations, we explored the effects of the surface diffusion and the interfacial structure. Furthermore, we demonstrated that the phase formation and morphology of Pt-Sn iNPs could be predicted and controlled according to our findings. These iNPs showed dramatically altered catalytic properties in the semi-hydrogenation of acetylene, emphasizing the importance of understanding the alloying mechanism of iNPs.

RESULTS

Characterization of $Pt/SnO_2@mSiO_2$ before Reaction

The $Pt/SnO_2@mSiO_2$ nano-reactor featured the well-encapsulated Pt/SnO_2 reactant pairs in the mesoporous silica shells. Figure 1A shows a typical HAADF-STEM image of the sample. The Pt particles in bright contrast had an average diameter of 4.0 ± 1.4 nm, derived from a histogram of size distribution shown in the inset. The SnO_2 particles in light-gray contrast could be found either side by side or as shells in a core-shell structure with Pt nanoparticles. The silica shells that surround the particles rendered in dark-gray contrast. Elemental mapping on a single capsule by energy-dispersive X-ray spectroscopy (EDS) further confirmed the well-encapsulated Pt/SnO_2, as shown in Figure S1. A reactant pair with a ~5 nm Pt particle (top) and a ~10 nm SnO_2 particle (bottom) was selected for *in situ* observation, as presented

[1]Ames Laboratory, US Department of Energy, Ames, IA 50011, USA

[2]Department of Mechanical and Energy Engineering, Southern University of Science and Technology, Shenzhen 518055, China

[3]Department of Chemistry, Iowa State University, Ames, IA 50011, USA

[4]Department of Materials Science and Engineering, Iowa State University, Ames, IA 50011, USA

[5]Lead Contact

*Correspondence: whuang@iastate.edu (W.H.), linzhou@ameslab.gov (L.Z.)

https://doi.org/10.1016/j.chempr.2019.02.026

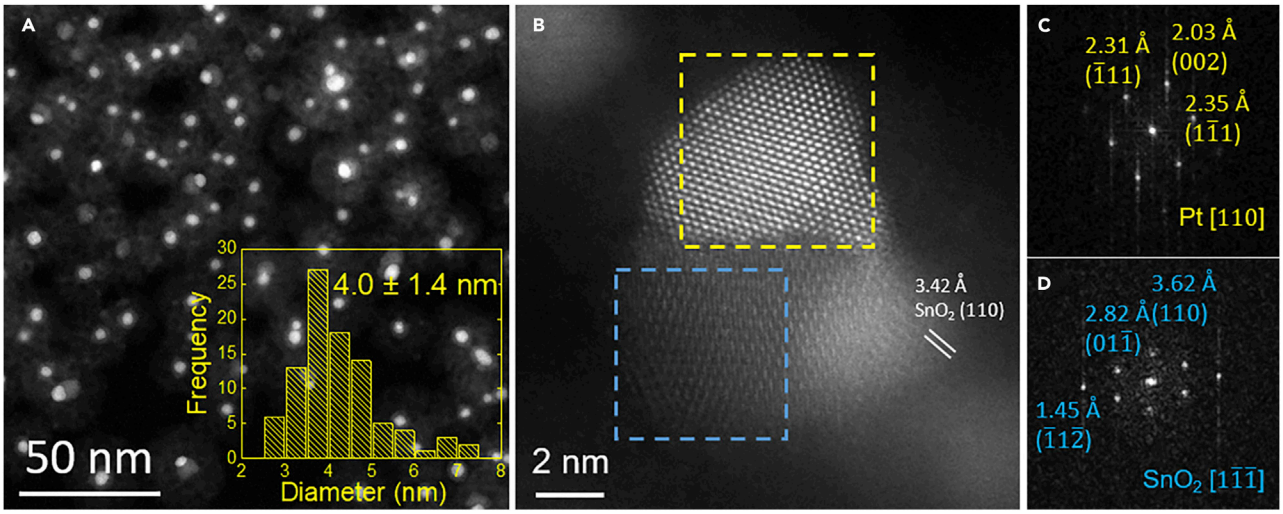

Figure 1. HAADF-STEM Images of $Pt/SnO_2@mSiO_2$ Nanoparticles before Reaction

(A) Typical low-magnification image showing Pt (bright), SnO_2 (light gray), and the SiO_2 shell (dark gray). A histogram of size distribution of Pt particles is shown in the inset, giving an average particle size of 4.0 ± 1.4 nm.

(B) The region for *in situ* STEM observation where Pt (upper) and SnO_2 (lower) coexisted side by side.

(C) FFT from the yellow box in (B) shows that the Pt particle was viewed along the [110] zone axis.

(D) FFT from the blue box in (B) shows that the viewing direction of SnO_2 is near $[1\bar{1}\bar{1}]$.

in Figure 1B. Fast Fourier transform (FFT) from the Pt region (Figure 1C) shows the *d*-spacings matching those of the face-centered cubic Pt. The gray region shows two discernible α-SnO_2 domains with different crystal orientations, one of which is near [11], as confirmed by the FFT (Figure 1D).

Pt_3Sn Formation and PtSn Nucleation at 350°C

The reaction between Pt and SnO_2 was successfully triggered by the electron beam at elevated temperature, yielding the formation of ordered Pt_3Sn and PtSn phases. Figure 2 shows a few selected frames at the early stage of the reaction. A shell with relatively dark contrast started to form around the Pt particle right after being exposed to the electron beam, as shown in Figures 2A, 2D, and 2G. The darker contrast of the shell compared with the Pt core indicates that the shell was rich in Sn. We attribute the appearance of this Sn-rich shell to the SnO_2 reduction initiated by the electron beam at 350°C. Interestingly, this shell was seen to rapidly "flow" on the particle surface throughout the reaction (see Video S1), indicative of the fast diffusivity of Sn via surface diffusion. As a result, an ordered Pt_3Sn phase formed at 3 s, as evident by the appearance of the superlattice spots in the FFT (Figure 2B). By applying masks in the Fourier space (marked by the yellow circles), we calculated a filtered real-space image containing only the information from Pt_3Sn by the inverse fast Fourier transform (IFFT) (Figure 2C). The IFFT image confirmed that the Pt_3Sn phase formed mainly at the surface of Pt. Similar Fourier filters were applied to the images at 18 s (Figure 2D) and 27 s (Figure 2G). The IFFT images in Figures 2F and 2I confirmed that Pt_3Sn became more prominent as the reaction proceeded.

Nucleation of the PtSn phase on the right corner of the Pt particle was observed after ~18 s, as highlighted by the yellow box in Figure 2D. The distance between the bright atomic columns with 6-fold symmetry, expected for PtSn, was measured as ~4.1 Å, matching the Pt-Pt spacing of hexagonal PtSn along [001] (see the atomic model in Figure 2K and a simulated HAADF image along [001] in Figure 2M). The PtSn nucleus and the parent Pt_3Sn phase follow a specific orientation

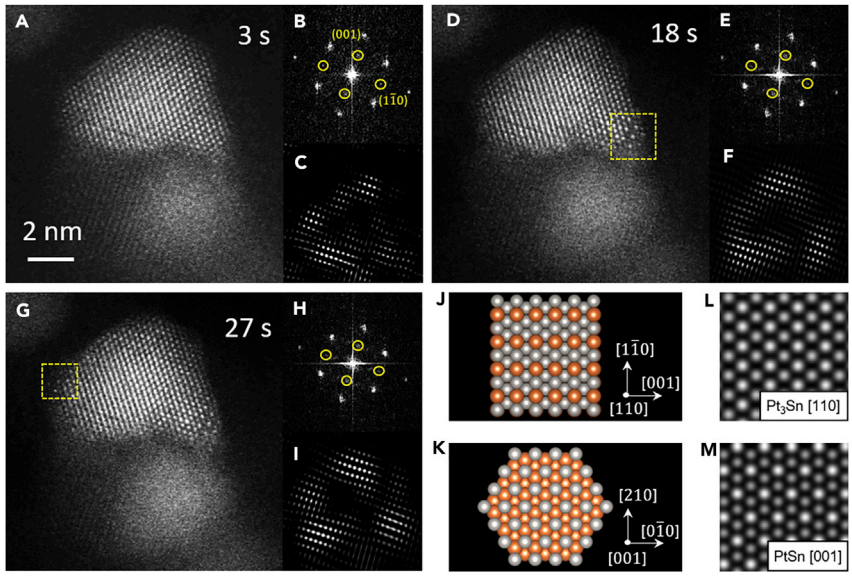

Figure 2. Selected Sequential HAADF-STEM Images of the mSiO$_2$-Encapsulated Pt/SnO$_2$ Reacting Pair in the Early Stage of Reaction at 350°C

(A, D, and G) Real-time video frames at 3 s (A), 18 s (D), and 27 s (G). The dashed boxes in (D) and (G) marked the PtSn nuclei.

(B, E, and H) Corresponding FFT patterns of the upper particle. (001) and (1$\bar{1}$0) superlattice spots of Pt$_3$Sn are highlighted by yellow circles.

(C, F, and I) IFFT images converted from (001) and (1$\bar{1}$0) superlattice spots of Pt$_3$Sn show the progression of the Pt$_3$Sn phase.

(J and K) Atomic models of Pt$_3$Sn along [110] (J) and PtSn along [001] (K). Silver spheres represent Pt atoms, which are smaller than the orange Sn atoms.

(L and M) Simulated HAADF images of Pt$_3$Sn along [110] (L) and PtSn along [001] (M), where Pt columns appear brighter than Sn columns because of the STEM Z contrast.

relationship: $(110)_{Pt_3Sn} \parallel (001)_{PtSn}$ and $[1\bar{1}0]_{Pt_3Sn} \parallel [210]_{PtSn}$. This configuration can be ascribed to the similar *d*-spacings of Pt$_3$Sn (002) (2.002 Å) and PtSn (110) (2.051 Å), giving a lattice misfit of only 2.4%. Another PtSn nucleus formed on the opposite corner was seen at 27 s, as shown in Figure 2G. Note that the nucleus formed with the same orientation preference described previously.

Growth of Pt$_3$Sn and PtSn

Using the aforementioned Fourier filters, we were able to track the evolution of Pt$_3$Sn. To do that, we superimposed the IFFT images from the Pt$_3$Sn (001) superlattice spots on the HAADF-STEM images with yellow color, as shown in Figure 3. The FFTs and the original IFFT images are presented in Figure S2. The Pt$_3$Sn phase mainly existed near the surface of the particle in the early stages (Figure 3A) and propagated gradually to the center of the particle as a result of Sn diffusion. The PtSn nucleus started to grow into the Pt$_3$Sn domain, leading to the migration of the $(1\bar{1}0)_{Pt_3Sn}/(100)_{PtSn}$ interface, seen at 69 s in Figure 3B. In contrast to the continuous growth of Pt$_3$Sn, the growth of PtSn was discontinuous, which included a reshuffle of atoms within a nanometer region. For example, at 79.5 s, the lattice fringes of Pt$_3$Sn in front of the PtSn nucleus suddenly disappeared, leaving a disordered region (Figure 3C, as marked by the dashed line). This region showed a darker contrast relative to the Pt/Pt$_3$Sn domains, suggesting a high concentration of Sn in the area. Pt columns with the hexagonal periodicity evolved from this Sn-rich region, as observed in the following frame (Figure 3D). This atomic-level rearrangement completed at 82.5 s, resulting in an ordered PtSn region on the right side of the particle (Figure 3E). When the Pt$_3$Sn phase was

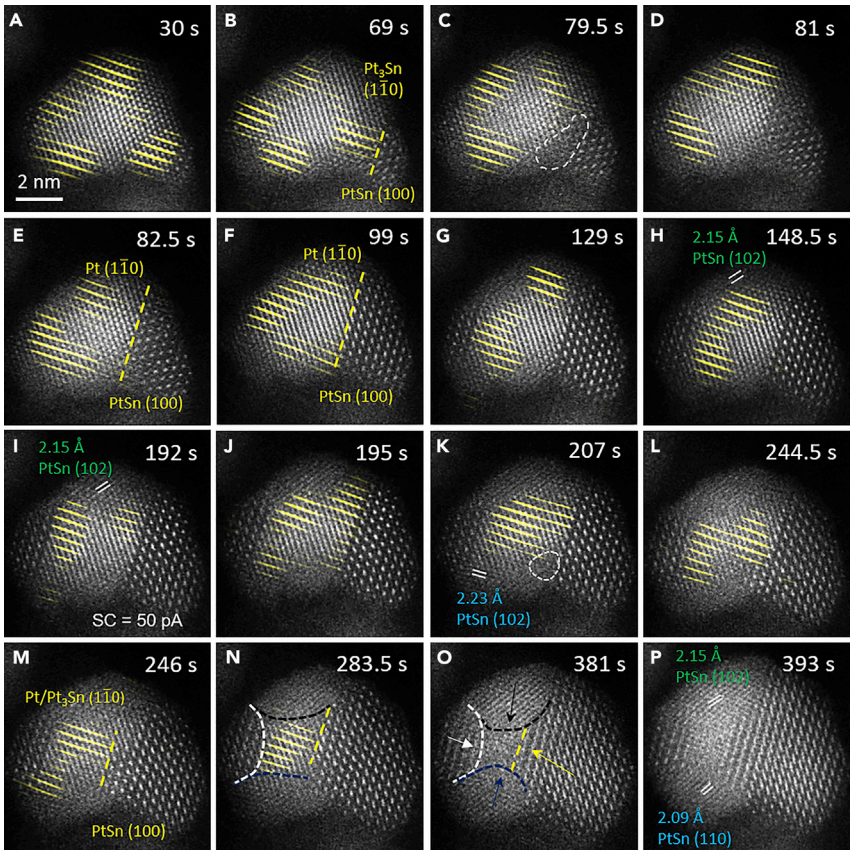

Figure 3. Sequential HAADF-STEM Images of the $mSiO_2$-Encapsulated Pt/SnO_2 Reactant Pair during the Reaction at 350°C Demonstrate the Growth of Pt_3Sn and PtSn

The images were superimposed with IFFT images (yellow color), generated from the superlattice spots of Pt_3Sn (001). FFT patterns and original IFFT images are shown in Figure S2.

depleted in front of the Pt_3Sn/PtSn interface, the progression of the PtSn domain arrested, possibly as a result of insufficient Sn supply. As can be seen in Figures 3E–3H, the Pt_3Sn and PtSn domains in the sample were nearly static, except for a slight growth of the other PtSn nucleus near the left edge (see Figure 3G). Assuming the reaction was limited by the supply of Sn, we increased the beam current from 30 to 50 pA at 192 s. Confirming our hypothesis that the electron beam is critical to the reduction of SnO_2, the formation of Pt_3Sn commenced (Figure 3I). At 195 s, the region in front of the interface was dominated by Pt_3Sn (Figure 3J). Similar to the previous growth sequence of PtSn out of Pt_3Sn + Sn (Figures 3C–3E), the disappearance of Pt_3Sn lattice was again observed at 207 s (Figure 3K), followed by the appearance of a disordered Sn-rich area (encircled by the dashed line). By 244.5 s, PtSn lattice emerged from the Sn-rich area (Figure 3L), resulting in the growth of the PtSn domain and the migration of the interface at 246 s (Figure 3M).

In addition, we noticed that a different PtSn grain formed in the top part of the particle at 148.5 s (Figure 3H). The lattice fringes were measured as ~2.15 Å, matching those of PtSn (102). The formation of this PtSn grain was also accompanied by the consumption of the Pt_3Sn phase. No orientation preference of this nucleation relative to the Pt particle was identified. This PtSn grain was hardly grown afterward. A similar phenomenon was observed at 283.5 s in the bottom part of the particle, as shown in Figure 3N. The particle at the time was composed of four distinct PtSn grains and one

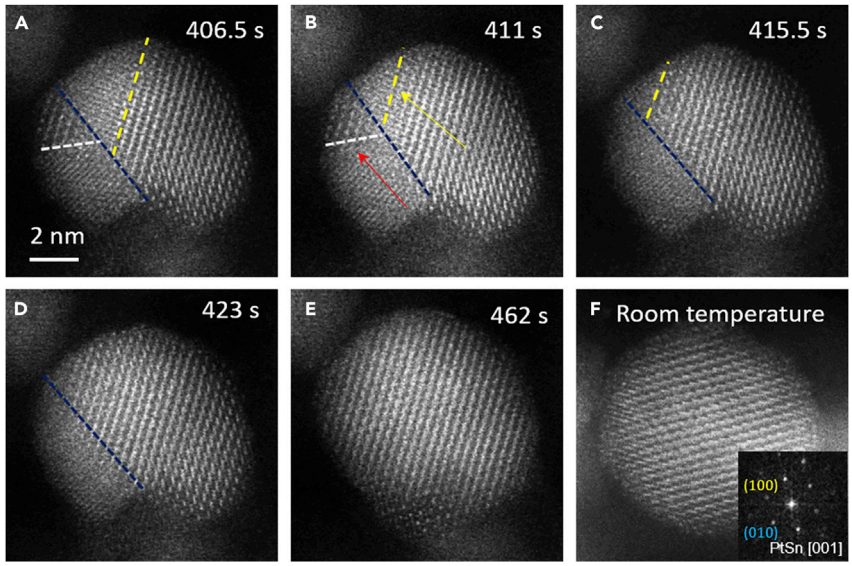

Figure 4. The Coalescence of PtSn Grains and the Formation of a Single-Crystalline PtSn iNP Monitored by *In Situ* STEM

(A–E) Sequential HAADF images taken at 350°C demonstrate the coalescence process of multiple PtSn grains. The dashed lines mark the grain boundaries, and arrows indicate the growth direction. (F) HAADF-STEM image of the single-crystalline PtSn taken after the sample was cooled down; FFT is shown in the inset.

unreacted Pt/Pt_3Sn grain. This tentative equilibrium was broken as annealing continued. At 381 s, the four PtSn grains started to grow toward the center of the particle, and the Pt_3Sn fringes disappeared (Figure 3O). Finally, the reaction ended up with four PtSn grains, between which boundaries were built up (Figure 3P).

Coalescence of the Multiple PtSn Grains

The final stage of the process involved the coalescence of PtSn grains. This process followed the classical sintering theory, in which the larger grains that have lower surface energy per unit volume tend to increase their size by consuming the smaller and higher surface energy grains.[37] As shown in Figures 4A–4D, the growth of the lower left and lower right grains toward the upper ones was first seen from 406.5 to 423 s, and the growth directions were indicated by arrows. Grain boundaries between them migrated and finally converged at the surface. This process was very fast—finished within only 16.5 s—resulting in a two-grain particle. Then, these two grains merged and transformed into a single grain (see Figure 4E). Note that from 423 s, the notch at the lower part of the particle started to be filled, along with the dissolution of a smaller particle in the vicinity (Figure 4D). This phenomenon is the typical Ostwald ripening that is often observed in the coalescence of nanoparticles.[38,39] A HAADF-STEM image of the sample (Figure 4F) was captured after it was cooled to room temperature. FFT in the inset reveals that the particle contained a single PtSn grain, which slightly rotated from the original [001] orientation during cooling. EDS mapping on the particle after the reaction (Figure S3) shows that Pt and Sn were uniformly distributed throughout the particle, indicating that the starting sample, Pt/SnO_2, was successfully converted to single crystalline PtSn.

Molecular Dynamics Simulation

To investigate the mechanism of the formation of ordered phases in the Pt/SnO_2@$mSiO_2$, we calculated the interfacial energy of Pt_3Sn/PtSn by using molecular

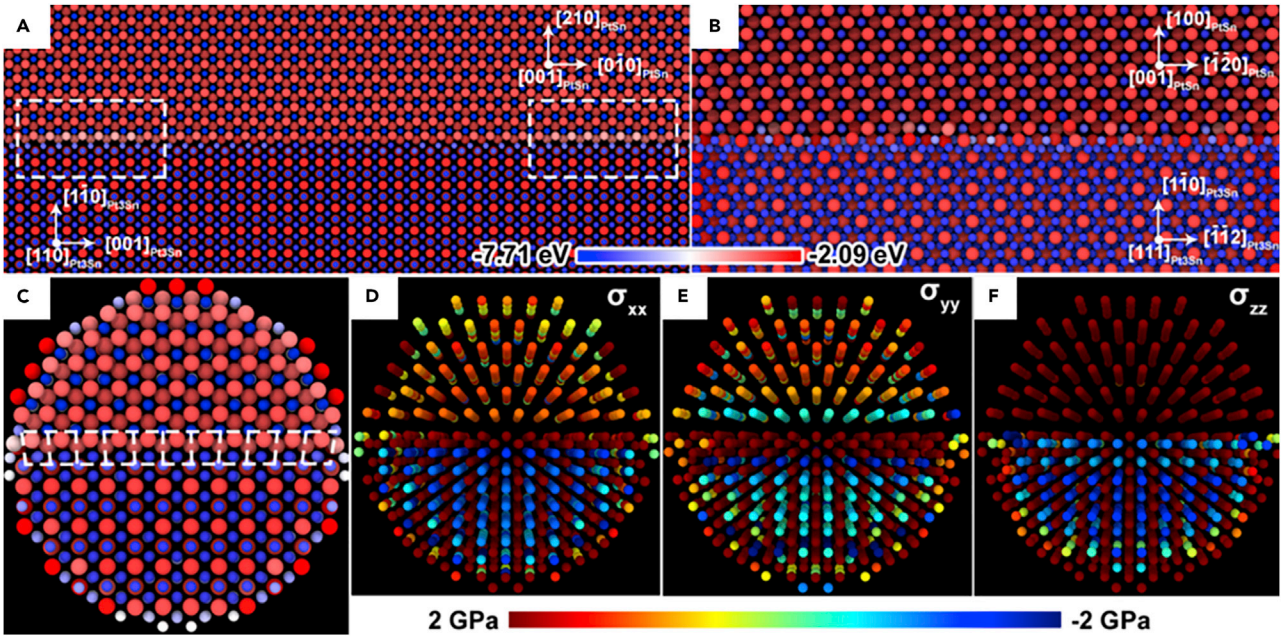

Figure 5. MD Results on Interfacial Structures and Stress Tensors of the Pt_3Sn/PtSn System

(A and B) Atomic structure of type 1 (A) and type 2 (B) interfaces (Pt atoms are rendered as smaller spheres than Sn). The upper crystal is PtSn, and the lower is Pt_3Sn. All atoms are colored by their cohesive energy (enthalpy per atom).

(C) Energetically preferred arrangement of a 5 nm PtSn/Pt_3Sn particle with a type 1 interface in the middle.

(D–F) Distribution of the stress tensors, σ_{xx} (D), σ_{yy} (E), and σ_{zz} (F), on Pt atoms, where Sn atoms were edited out for easy visualization.

dynamics (MD) simulations. Two types of interfaces were investigated: (1) $(110)_{Pt_3Sn} \parallel (001)_{PtSn}$ and $[1\bar{1}0]_{Pt_3Sn} \parallel [210]_{PtSn}$, which matches the STEM observation and is hereafter referred to as the type 1 interface; and (2) $(111)_{Pt_3Sn} \parallel (001)_{PtSn}$ and $[110]_{Pt_3Sn} \parallel [100]_{PtSn}$, the type 2 interface, which obeys the conventional interfacial relation between face-centered cubic and hexagonal close-packed crystals.[32] Note that the type 2 interface gave a lattice misfit of 17.6%, 7.3 times larger than that of the type 1 interface. The atomic configurations of type 1 and type 2 interfaces are shown in Figures 5A and 5B, respectively, and the atoms are colored by their cohesive energy (enthalpy per atom). The simulated model for the type 1 interface (Figure 5A) yielded an interfacial structure that was exactly the same as the *in situ* STEM results, except for some defected regions caused by the lattice misfit (marked by the dashed box). The interfacial energy for this configuration was as low as 0.459 J/m^2. The Pt atoms at the interface were all in their low-energy state, and the strongest cohesive energy was calculated to be −6.53 eV. For the type 2 interface (Figure 5B), the calculated interfacial energy was 2.47 J/m^2, 5.4 times larger than that of type 1. In addition, the distribution of the cohesive energy of atoms appeared to be random. The strongest cohesive energy of Pt atoms at the interface was −5.91 eV, consistent with its high interfacial energy and large lattice misfit. The result indicates that the type 1 interface is energetically more favorable than the type 2 interface.

To account for the situation in the nanoparticles, we extracted a 5 nm sphere-shaped particle from the defect-free region in Figure 5A. A section view of the resulting atomic arrangement is presented in Figure 5C, in which all atoms are colored by the same cohesive energy scale used in Figures 5A and 5B. Note that the atoms on the surface of the particle had slightly higher cohesive energy than the internal ones, indicating that the elastic strain induced by the lattice misfit was released to

the particle surface. However, the misfit cannot be eliminated entirely at the interface, as indicated by the dashed lines in Figure 5C, where the Pt frames were obviously distorted. During the transformation from Pt_3Sn to PtSn, the Pt atoms were substituted by Sn in the Pt_3Sn phase. The excess energy induced by the substitution process can be assessed by combining the atomic stress field and the elasticity theory.[40,41] Because Sn has a larger atomic radius than Pt, the substitution of Pt by Sn induces a dilatational strain at the original Pt site, which can be represented by a dilatational volume, V_{Sn} ($Å^3$ per Sn atom), with a positive value. The excess energy (binding energy) for the substitution can be expressed as $E_b = -V_{Sn} \cdot \sigma_{ij}^{Pt}$, where σ_{ij}^{Pt} is the local stress field on the Pt site.[42] Apparently, a tensile stress field that gives a positive value of σ_{ij}^{Pt} will result in a negative binding energy and *vice versa*. It can be seen in the calculated stress tensors (Figures 5D–5F) that the Pt atoms near the interface-affected region of Pt_3Sn were always subjected to relatively high tensile stress, indicating that these atoms are energetically preferable for the substitution by Sn. The result reveals that the unique interfacial structure of Pt_3Sn/PtSn induces tensile stress on the Pt atoms at the interface and serves as the driving force for the $Pt_3Sn \rightarrow$ PtSn transformation.

DISCUSSION

The above *in situ* observation demonstrated that the reaction between Pt and SnO_2 in the Pt/SnO_2@mSiO_2 nano-reactor encompasses consecutive transformations: the Pt_3Sn phase was first formed at the surface of the Pt particle once the SnO_2 was reduced; further reducing SnO_2 resulted in the transformation of Pt_3Sn to PtSn. At the beginning of the reaction, the Pt surface facilitated diffusion of free Sn, as evident by the "flowing shell" on Pt (see Video S1). This surface-mediated Sn diffusion was responsible for the fast formation of Pt_3Sn, which was seen right after free Sn was generated (Figure 2). The continuous growth of Pt_3Sn suggests that this process is mainly controlled by Sn diffusion. PtSn nucleation was first seen on the particle corner (Figure 2D), where the nucleus could minimize its critical volume, V^*.[32] The energy barrier was hence lowered, given by $\Delta G^* = 1/2V^* \cdot \Delta G_V$, where ΔG_V is the difference of the free energies per unit volume of PtSn and Pt_3Sn. More importantly, with a unique coherent interface, $(110)_{Pt_3Sn} \parallel (001)_{PtSn}$ and $[1\bar{1}0]_{Pt_3Sn} \parallel [210]_{PtSn}$, the interfacial energy was minimized. Therefore, the energy barrier was further reduced, given that $V^* \propto \gamma^3$, where γ is the interfacial energy.[32] In order for the PtSn nucleus to grow and the interface to migrate, a net flux of Sn atoms from the Pt_3Sn phase is required. The driving force for this uphill diffusion was the tensile stress (induced by the interface) on Pt sites. The Sn atoms in front of the interface were pulled toward the PtSn side, leading to the substitution of Pt by Sn and the formation of PtSn. When the region in front of the interface was depleted of Sn, e.g., after 82.5 s of the reaction (see Figures 3E–3H), the transformation halted because of insufficient Sn supply. Then, the beam current was increased to speed up the reduction of SnO_2 and hence secure the Sn diffusion. As a result, we were able to resume the formation of Pt_3Sn, as well as its transformation to PtSn. Therefore, Sn diffusion plays a crucial role in the formation of ordered phases in the Pt-Sn system.

Moreover, particle size also alters the reaction dynamics. We conducted similar observation on ~10 and ~15 nm Pt particles, and the selected sequential HAADF-STEM images are presented in Figures S4 and S5, respectively. It can be seen that reaction speed slowed down as the Pt size increased, e.g., Pt_3Sn formed at 3 min (Figure S4B) and PtSn nucleation occurred at 5 min (Figure S4C) in the ~10 nm particle, whereas the formation of Pt_3Sn was noticed at 18 min in the ~15 nm particle (Figure S5B), and its transformation to PtSn was observed at 23 min (Figure S5C).

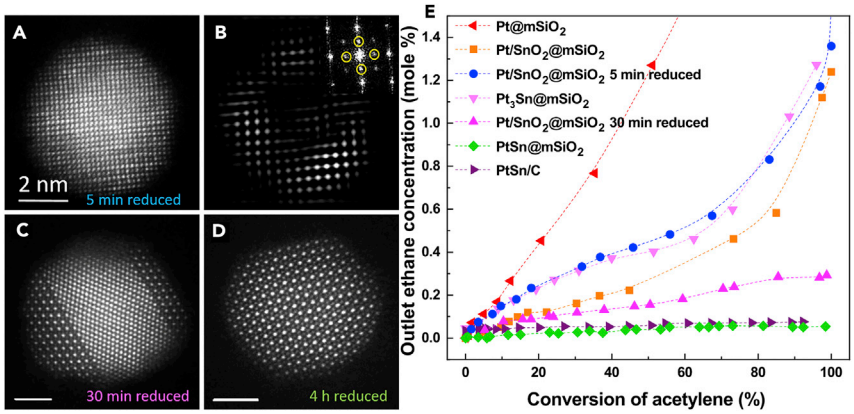

Figure 6. Controlled Phase Formation of Pt-Sn iNPs and Their Catalytic Performance for Acetylene Semi-hydrogenation

(A–D) Representative HAADF-STEM images of $Pt/SnO_2@mSiO_2$ reduced in flowing hydrogen at 300°C for 5 min (A), 30 min (C), and 4 h (D). (B) IFFT image from (A) generated by the superlattice spots of Pt_3Sn (circled in the inset).

(E) Concentration of ethane measured at the reactor outlet versus acetylene conversion for the synthesized Pt-Sn iNP catalysts. 0% ethane corresponds to the highest selectivity of acetylene hydrogenation. The reactant gas mixture contains 13.35 mL/min He, 1.5 mL/min H_2, 15 mL/min C_2H_4, and 0.15 mL/min C_2H_2 at 1 bar.

Nevertheless, the reaction followed the same pathway as we discussed in the ~5 nm particle, suggesting that the particle size mainly affects Sn diffusion because the bigger particle has a lower diffusivity.[43] In addition, stacking faults were observed in the ~10 nm particle (Figure S4A), which seemed to facilitate Sn diffusion (Figure S4D). As a result, the PtSn front propagated preferentially along the defective region, which was slightly rich in Sn. However, the stacking faults eventually annihilated as the reaction proceeded (Figure S4E). Because of the short lifetime of this structural imperfection, its effect on the reaction dynamics is likely to be subordinate.

The above results also provide possibilities for controlling the formation of ordered phases in iNPs by accommodating diffusion of the second element, e.g., at different reaction conditions. As a proof of concept, we demonstrate that controlled phase formation and morphology of Pt-Sn iNPs can be achieved by thermal reduction of $Pt/SnO_2@mSiO_2$ at 300°C in flowing hydrogen for varied time. Figure S6 presents X-ray diffraction (XRD) profiles of the starting $Pt/SnO_2@mSiO_2$ and the samples reduced for 5 min, 30 min, and 4 h, showing gradual transformation of $Pt \rightarrow Pt_3Sn \rightarrow PtSn$. The crystallite size was estimated to be 4–5 nm from the XRD results (Table S1), in agreement with the HAADF-STEM images in Figures 6A–6D, S7, and S8. Particles with Pt_3Sn-enriched surface were obtained in the sample reduced for 5 min given that Sn diffusion was limited (Figures 6A, 6B, and S7). The $Pt_3Sn/PtSn$ bicrystal structure with the coherent interface was reproduced by allowing Sn diffusion for 30 min (Figures 6C and S8). Full conversion of Pt/SnO_2 to PtSn phase was reached in the sample reduced for 4 h (Figure 6D).

The above Pt-Sn iNPs were tested for semi-hydrogenation of acetylene with a reactant gas mixture consisting 50% ethylene, 0.5% acetylene, and 5% H_2. $Pt@mSiO_2$ nanoparticles as well as pure $Pt_3Sn@mSiO_2$ and carbon-supported PtSn/C samples were also examined for comparison. A highly selective catalyst will remove trace amounts of acetylene from ethylene and simultaneously avoid the hydrogenation

of ethylene to ethane—the process is important for the polyethylene industry.[6] The produced ethane concentration as a function of acetylene conversion is plotted in Figure 6E for these catalysts, and different catalytic behaviors were evident. Pt@mSiO$_2$ showed the worst semi-hydrogenation selectivity among all the catalysts because Pt is an excellent ethylene hydrogenation catalyst. Pt/SnO$_2$@mSiO$_2$ without reduction displayed better selectivity than Pt@mSiO$_2$. Interestingly, the 5-min-reduced iNPs showed worse semi-hydrogenation selectivity than Pt/SnO$_2$@mSiO$_2$ because of the formation of the Pt$_3$Sn-enriched surface. Indeed, the pure Pt$_3$Sn@mSiO$_2$ gave results very similar to those of the 5-min-reduced sample, confirming this structure-induced change on the catalytic performance. Given that the PtSn-enriched surface was constructed after 30 min of reduction (Pt$_3$Sn/PtSn bicrystal structure), the semi-hydrogenation selectivity of the catalyst was substantially improved. The PtSn catalyst obtained from the full conversion of Pt/SnO$_2$@mSiO$_2$ exhibited the best selectivity, whereby only 0.05 mol % ethane was generated at 100% conversion of acetylene. In addition, these catalysts were stable upon the reaction, giving identical activity and selectivity in the second run (Figure S11). XRD (Figure S6) and STEM observations (Figures S9 and S10) on the used samples revealed no essential changes in the structure of these iNPs. These reaction and characterization results strongly support that it is possible to achieve phase and catalysis control on the basis of the understanding of the Pt/SnO$_2$ → PtSn transformation process obtained from the *in situ* STEM studies. Note that there may be a large number of Sn–O–Si bonds in mSiO$_2$-encapsulated iNPs. It was reported that these bonds strongly influence the catalytic properties in hydrogenations.[44] To exclude the effect of Sn–O–Si bonds, we prepared carbon-supported PtSn/C iNPs and tested their catalytic performance for the acetylene semi-hydrogenation. As shown in Figure 6E, the selectivity of PtSn/C showed a similar trend as PtSn@mSiO$_2$, indicating that the effect of Sn–O–Si bonds, if any, is less dominant. These results indicate that the catalytic properties of Pt-Sn iNPs can be tailored according to the atomic-level understanding of their alloying mechanism, providing insightful guidance on design and synthesis of intermetallic catalysts.

EXPERIMENTAL PROCEDURES

Synthesis of Pt/SnO$_2$@mSiO$_2$ Nano-reactor

The monometallic Pt@mSiO$_2$ was prepared according to previous literature[15,33,45] with modification. In a typical synthesis, 52 mg tetradecyltrimethylammonium bromide (TTAB, ≥99%, Sigma-Aldrich) was added to an aqueous solution (20 mL, 0.750 mM) of H$_2$PtCl$_6$ (Acros Organics, 40% Pt) and sonicated until dissolved. The reaction mixture was heated in an oil bath at 60°C for 10 min, and a freshly prepared aqueous solution (26 mL, 10 mM) of sodium borohydride (Alfa Aesar, 98%) was then added quickly. After the mixture was stirred vigorously for 10 min, a dark-brown colloidal solution of Pt NPs was observed, and an aqueous solution (0.1 mL, 1 M) of sodium hydroxide was added. Next, 1 mL of 10% tetraethylorthosilicate (TEOS, Aldrich, reagent grade, 98%) solution in ethanol was added dropwise with vigorous stirring. After 6 h, the solution was allowed to cool to room temperature, and 20 mL ethanol was added. The solution was then centrifuged at 8,000 rpm, and the coated NPs were collected and dispersed in methanol. The surfactant was removed via an acidic methanol refluxing session (6% hydrochloric acid solution) at 90°C for 24 h. To make Pt/SnO$_2$@mSiO$_2$, the above Pt@mSiO$_2$ solution was centrifuged and redispersed in 75 mL of tetraethylene glycol (Alfa Aesar, 99%) in a 250 mL two-neck flask. SnCl$_2$·2H$_2$O (Alfa Aesar, 98%) was added to the solution with a molar ratio of Pt:Sn = 1:1. The solution was heated at 280°C for 2 h, and then excess acetone was added after it cooled down. The solution was then centrifuged at 14,000 rpm, and the solid

was dried and calcined at 500°C for 4 h for the removal of any remaining organic residues. $Pt_3Sn@mSiO_2$ was made in a similar way except that the initial Pt:Sn ratio was changed to 3:1. After calcination, the $Pt/SnO_2@mSiO_2$ sample was reduced at 600°C for 4 h to make the Pt_3Sn phase. PtSn/C was made with a successive impregnation method. Proper amount of H_2PtCl_6 was dissolved in 2 mL H_2O, and 50 mg carbon nanotube (multiwall, –COOH functionalized) was dispersed in it. This solution was stirred in an 80°C oil bath until dry, and then the sample was reduced at 200°C for 2 h to form Pt/C. $SnCl_2$ was then similarly impregnated with acetone as the solvent, dried at room temperature, and reduced at 500°C to form PtSn/C.

Transmission Electron Microscopy

STEM observation was performed with an FEI Titan Themis 300 probe-corrected scanning transmission electron microscope under an accelerating voltage of 200 kV. A gun monochromator was equipped to enable continuous tuning of the beam current for scanning. The $Pt/SnO_2@mSiO_2$ powder was dispersed in ethanol and sonicated for 30 min before being dropcast onto the FEI NanoEx-i/v MEMS chip,[46] which was equipped with a microheater for rapid and precise heating of the sample. The chip was mounted to the FEI NanoEx-i/v heating and biasing holder, which enabled *in situ* heating up to 1,200°C inside the microscope. During observation, the sample was heated to 350°C and allowed to stabilize for 10 min. The electron beam was blanked during the temperature ramp and stabilization and unblanked afterward, at which time a video started to record (set as $t = 0$ s). The initial beam current was set to 30 pA so that the reaction would be slow enough to be monitored. The video, captured with a frame rate of 1.5 s within a collection angle of 99–200 mrad, was sped up 15 times, annotated along with a real-time scale, and attached in Video S1. Image simulation was carried out by QSTEM[47] software according to the multislice technique with the same parameter configuration as the actual microscope.

Theoretical Calculations

MD simulations were performed with LAMMPS software.[48] The interatomic interaction between Pt and Sn was described by a modified embedded-atom method (MEAM) potential that was tabulated by fitting the experimental and first-principle calculation results of the Pt-Sn system.[49] The bicrystal models were constructed with the three-dimensional Born-von Karman periodic boundary condition (PBC), which eliminated the surface effect. Rigid body transitions were performed on the basis of a 10 × 10 grid that mapped the periodic lengths along the width and thickness axis on the plane of interface.[50] The resulting atomic structures of all candidates were optimized by a non-linear congregate gradient method with an energy convergence criterion of 0.01 meV. The configuration with the lowest interfacial energy was selected for comparison. To build a bicrystal nanoparticle, a 5 nm sphere-shaped particle was extracted from the interface model and fully relaxed and optimized until its hydrostatic pressure became zero and the total energy became convergence. The stress tensors of each atom were obtained by the algorithm in LAMMPS software. More computational details can be found in the Supplemental Information.

Catalytic Evaluation of Acetylene Semi-hydrogenation

Semi-hydrogenation of acetylene was performed in a U-tube quartz reactor. A 4 mg catalyst (8 mg for PtSn/C to adjust for less surface area) was weighed and mixed with 200 mg quartz sand. A reactant gas mixture consisting of 13.35 mL/min He, 1.5 mL/min H_2, 15 mL/min C_2H_4, and 0.15 mL/min C_2H_2 at 1 bar was flowed through the catalyst during reaction, and the outlet gas composition was characterized by an HP 5890 gas chromatography equipped with a capillary column (HP PLOT Q,

30 m × 25 mm × 0.25 μm) and a flame ionization detector. To obtain full conversion, the reactions were allowed to run from 25°C to 100°C for Pt@$mSiO_2$, 60°C to 200°C for unreduced Pt/SnO_2@$mSiO_2$, 100°C to 200°C for 5-min-reduced Pt/SnO_2@$mSiO_2$ and Pt_3Sn@$mSiO_2$, and 50°C to 260°C for 30-min-reduced Pt/SnO_2@$mSiO_2$, PtSn@$mSiO_2$, and PtSn/C. The temperature ramping rate was controlled at 0.2°C/min for all the catalysts.

SUPPLEMENTAL INFORMATION

Supplemental Information can be found online at https://doi.org/10.1016/j.chempr.2019.02.026.

ACKNOWLEDGMENTS

This work was supported in part by Laboratory Directed Research and Development funds through the Ames Laboratory and by the US Department of Energy, Office of Science, Basic Energy Sciences, Materials Sciences and Engineering Division. The Ames Laboratory is operated for the US Department of Energy by Iowa State University under contract no. DE-AC02-07CH11358. All TEM and related work were performed with instruments in the Sensitive Instrument Facility in the Ames Laboratory. W.H., M.C., and R.V.M.-G. gratefully acknowledge the support from the National Science Foundation through award no. 1808239. S.W. gratefully acknowledges the support from the National Science Foundation through award no. CMMI-1406462.

AUTHOR CONTRIBUTIONS

L.Z. and W.H. designed and initiated the work. T.M. and L.Z. carried out the TEM work and analyzed the results. M.C. and R.V.M.-G. fabricated the nano-reactor. M.C. performed the thermal reduction, XRD, and catalytic reaction studies. S.W. performed the MD simulations. L.-L.W., D.D.J., and M.J.K. advised on alloying and interfacial phenomena and the analysis of observations. All authors contributed to the discussion of the results and writing of the manuscript.

DECLARATION OF INTERESTS

The authors declare no competing interests.

Received: July 10, 2018
Revised: February 8, 2019
Accepted: February 26, 2019
Published: March 28, 2019

REFERENCES AND NOTES

1. Wang, D., Xin, H.L., Hovden, R., Wang, H., Yu, Y., Muller, D.A., DiSalvo, F.J., and Abruña, H.D. (2013). Structurally ordered intermetallic platinum–cobalt core–shell nanoparticles with enhanced activity and stability as oxygen reduction electrocatalysts. Nat. Mater. *12*, 81–87.

2. Freakley, S.J., He, Q., Harrhy, J.H., Lu, L., Crole, D.A., Morgan, D.J., Ntainjua, E.N., Edwards, J.K., Carley, A.F., Borisevich, A.Y., et al. (2016). Palladium-tin catalysts for the direct synthesis of H_2O_2 with high selectivity. Science *351*, 965–968.

3. Gong, Y., Wu, J., Kitano, M., Wang, J., Ye, T.N., Li, J., Kobayashi, Y., Kishida, K., Abe, H., Niwa, Y., et al. (2018). Ternary intermetallic LaCoSi as a catalyst for N_2 activation. Nat. Catal. *1*, 178–185.

4. Bu, L., Zhang, N., Guo, S., Zhang, X., Li, J., Yao, J., Wu, T., Lu, G., Ma, J.Y., Su, D., et al. (2016). Biaxially strained PtPb/Pt core/shell nanoplate boosts oxygen reduction catalysis. Science *354*, 1410–1414.

5. Chen, C., Kang, Y., Huo, Z., Zhu, Z., Huang, W., Xin, H.L., Snyder, J.D., Li, D., Herron, J.A., Mavrikakis, M., et al. (2014). Highly crystalline multimetallic nanoframes with three-dimensional electrocatalytic surfaces. Science *343*, 1339–1343.

6. Studt, F., Abild-Pedersen, F., Bligaard, T., Sørensen, R.Z., Christensen, C.H., and Nørskov, J.K. (2008). Identification of non-precious metal alloy catalysts for selective hydrogenation of acetylene. Science *320*, 1320–1322.

7. Armbrüster, M., Kovnir, K., Friedrich, M., Teschner, D., Wowsnick, G., Hahne, M., Gille, P., Szentmiklósi, L., Feuerbacher, M., Heggen, M., et al. (2012). $Al_{13}Fe_4$ as a low-cost alternative for palladium in heterogeneous hydrogenation. Nat. Mater. *11*, 690–693.

8. Feng, Q., Zhao, S., Wang, Y., Dong, J., Chen, W., He, D., Wang, D., Yang, J., Zhu, Y., Zhu, H., et al. (2017). Isolated single-atom Pd sites in intermetallic nanostructures: high catalytic selectivity for semihydrogenation of alkynes. J. Am. Chem. Soc. *139*, 7294–7301.

9. Feng, Q., Zhao, S., He, D., Tian, S., Gu, L., Wen, X., Chen, C., Peng, Q., Wang, D., and Li, Y. (2018). Strain engineering to enhance the electrooxidation performance of atomic-layer Pt on intermetallic Pt_3Ga. J. Am. Chem. Soc. *140*, 2773–2776.

10. Li, Z., Yu, L., Milligan, C., Ma, T., Zhou, L., Cui, Y., Qi, Z., Libretto, N., Xu, B., Luo, J., et al. (2018). Two-dimensional transition metal carbides as supports for tuning the chemistry of catalytic nanoparticles. Nat. Commun. *9*, 5258.

11. Hao, R., Xing, R., Xu, Z., Hou, Y., Gao, S., and Sun, S. (2010). Synthesis, functionalization, and biomedical applications of multifunctional magnetic nanoparticles. Adv. Mater. *22*, 2729–2742.

12. Furukawa, S., and Komatsu, T. (2017). Intermetallic compounds: promising inorganic materials for well-structured and electronically modified reaction environments for efficient catalysis. ACS Catal. *7*, 735–765.

13. Voss, M.R., Busse, H., and Koel, B.E. (1998). Adsorption of thermal D atoms on Sn/Pt(111) surface alloys. Surf. Sci. *414*, 330–340.

14. Wu, Z., Bukowski, B.C., Li, Z., Milligan, C., Zhou, L., Ma, T., Wu, Y., Ren, Y., Ribeiro, F.H., Delgass, W.N., et al. (2018). Changes in catalytic and adsorptive properties of 2 nm Pt_3Mn nanoparticles by subsurface atoms. J. Am. Chem. Soc. *140*, 14870–14877.

15. Zhao, E.W., Maligal-Ganesh, R., Du, Y., Zhao, T.Y., Collins, J., Ma, T., Zhou, L., Goh, T.W., Huang, W., and Bowers, C.R. (2018). Surface-mediated hyperpolarization of liquid water from parahydrogen. Chem *4*, 1387–1403.

16. Markiewicz, W., Mains, E., Vankeuren, R., Wilcox, R., Rosner, C., Inoue, H., Hayashi, C., and Tachikawa, K. (1977). A 17.5 tesla superconducting concentric Nb3Sn and V3Ga magnet system. IEEE Trans. Magn. *13*, 35–37.

17. Ma, T., Long, Y., Liu, R., Fu, B., Zhang, H., Ye, R., and Chang, Y. (2010). Study on the homogeneity of hydrogenation for $LaFe_{11.5}Si_{1.5}$ intermetallic compound. Mater. Lett. *64*, 2520–2522.

18. Wang, C., Long, Y., Ma, T., and Zhang, H. (2011). Magnetocaloric effect and magnetic properties of $La_{0.9}Ce_{0.1}(Fe_{0.99}Mn_{0.01})_{11.6}Si_{1.4}H_{1.6}$ compound. J. Rare Earths *29*, 474–476.

19. Palacín, M.R. (2009). Recent advances in rechargeable battery materials: a chemist's perspective. Chem. Soc. Rev. *38*, 2565–2575.

20. Jain, A., Kawasako, E., Miyaoka, H., Ma, T., Isobe, S., Ichikawa, T., and Kojima, Y. (2013). Destabilization of LiH by Li insertion into Ge. J. Phys. Chem. C *117*, 5650–5657.

21. Oriani, R.A. (1954). Thermodynamics of ordering alloys, II. The gold-copper system. Acta Metall. *2*, 608–615.

22. Bray, A.J. (1994). Theory of phase-ordering kinetics. Adv. Phys. *43*, 357–459.

23. H. Baker, and H. Okamoto, eds. (1992). ASM Handbook Volume 3: Alloy Phase Diagrams (ASM International).

24. Volokitin, Y., Sinzig, J., de Jongh, L.J., Schmid, G., Vargaftik, M.N., and Moiseevi, I.I. (1996). Quantum-size effects in the thermodynamic properties of metallic nanoparticles. Nature *384*, 621–623.

25. Haner, A.N., Ross, P.N., and Bardi, U. (1991). The surface structure and composition of <111> and <100> oriented single crystals of the ordered alloy Pt_3Sn. Surf. Sci. *249*, 15–20.

26. Rodriguez, J.A., Jirsak, T., Chaturvedi, S., and Hrbek, J. (1998). Surface chemistry of SO_2 on Sn and Sn/Pt(111) alloys: Effects of metal-metal bonding on reactivity toward sulfur. J. Am. Chem. Soc. *120*, 11149–11157.

27. Desario, D.Y., and Disalvo, F.J. (2014). Ordered intermetallic Pt–Sn nanoparticles: exploring ordering behavior across the bulk phase diagram. Chem. Mater. *26*, 2750–2757.

28. Cable, R.E., and Schaak, R.E. (2006). Reacting the unreactive: a toolbox of low-temperature solution-mediated reactions for the facile interconversion of nanocrystalline intermetallic compounds. J. Am. Chem. Soc. *128*, 9588–9589.

29. Maligal-Ganesh, R.V., Xiao, C., Goh, T.W., Wang, L.L., Gustafson, J., Pei, Y., Qi, Z., Johnson, D.D., Zhang, S., Tao, F., et al. (2016). A ship-in-a-bottle strategy to synthesize encapsulated intermetallic nanoparticle catalysts: exemplified for furfural hydrogenation. ACS Catal. *6*, 1754–1763.

30. Wang, X., Altmann, L., Stöver, J., Zielasek, V., Bäumer, M., Al-Shamery, K., Borchert, H., Parisi, J., and Kolny-Olesiak, J. (2013). Pt/Sn intermetallic, core/shell and alloy nanoparticles: colloidal synthesis and structural control. Chem. Mater. *25*, 1400–1407.

31. Yan, Y., Du, J.S., Gilroy, K.D., Yang, D., Xia, Y., and Zhang, H. (2017). Intermetallic nanocrystals: Syntheses and catalytic applications. Adv. Mater. *29*, 1605997.

32. Porter, D.A., and Easterling, K.E. (1992). Phase Transformation in Metals and Alloys, Second Edition (CRC Press).

33. Joo, S.H., Park, J.Y., Tsung, C.K., Yamada, Y., Yang, P., and Somorjai, G.A. (2009). Thermally stable Pt/mesoporous silica core-shell nanocatalysts for high-temperature reactions. Nat. Mater. *8*, 126–131.

34. Chi, M., Wang, C., Lei, Y., Wang, G., Li, D., More, K.L., Lupini, A., Allard, L.F., Markovic, N.M., and Stamenkovic, V.R. (2015). Surface faceting and elemental diffusion behaviour at atomic scale for alloy nanoparticles during in situ annealing. Nat. Commun. *6*, 8925.

35. He, K., Zhang, S., Li, J., Yu, X., Meng, Q., Zhu, Y., Hu, E., Sun, K., Yun, H., Yang, X.Q., et al. (2016). Visualizing non-equilibrium lithiation of spinel oxide via in situ transmission electron microscopy. Nat. Commun. *7*, 11441.

36. Dai, S., You, Y., Zhang, S., Cai, W., Xu, M., Xie, L., Wu, R., Graham, G.W., and Pan, X. (2017). In situ atomic-scale observation of oxygen-driven core-shell formation in Pt_3Co nanoparticles. Nat. Commun. *8*, 204.

37. Pan, J., Le, H., Kucherenko, S., and Yeomans, J.A. (1998). A model for the sintering of spherical particles of different sizes by solid state diffusion. Acta Mater. *46*, 4671–4690.

38. Zheng, H., Smith, R.K., Jun, Y.W., Kisielowski, C., Dahmen, U., and Alivisatos, A.P. (2009). Observation of single colloidal platinum nanocrystal growth trajectories. Science *324*, 1309–1312.

39. Li, D., Nielsen, M.H., Lee, J.R.I., Frandsen, C., Banfield, J.F., and De Yoreo, J.J. (2012). Direction-specific interactions control crystal growth by oriented attachment. Science *336*, 1014–1018.

40. Hanlumyuang, Y., Gordon, P.A., Neeraj, T., and Chrzan, D.C. (2010). Interactions between carbon solutes and dislocations in bcc iron. Acta Mater. *58*, 5481–5490.

41. Wang, S., Takahashi, K., Hashimoto, N., Isobe, S., and Ohnuki, S. (2013). Strain field of interstitial hydrogen atom in body-centered cubic iron and its effect on hydrogen–dislocation interaction. Scr. Mater. *68*, 249–252.

42. Cochardt, A.W., Schoek, G., and Wiedersich, H. (1955). Interaction between dislocations and interstitial atoms in body-centered cubic metals. Acta Metall. *3*, 533–537.

43. Jiang, Q., Zhang, S.H., and Li, J.C. (2004). Grain size-dependent diffusion activation energy in nanomaterials. Solid State Commun. *130*, 581–584.

44. Wang, L., Guan, E., Zhang, J., Yang, J., Zhu, Y., Han, Y., Yang, M., Cen, C., Fu, G., Gates, B.C., et al. (2018). Single-site catalyst promoters accelerate metal-catalyzed nitroarene hydrogenation. Nat. Commun. *9*, 1362.

45. Pei, Y., Maligal-Ganesh, R.V., Xiao, C., Goh, T.W., Brashler, K., Gustafson, J.A., and Huang, W. (2015). An inorganic capping strategy for the seeded growth of versatile bimetallic nanostructures. Nanoscale *7*, 16721–16728.

46. Mele, L., Konings, S., Dona, P., Evertz, F., Mitterbauer, C., Faber, P., Schampers, R., and Jinschek, J.R. (2016). A MEMS-based heating holder for the direct imaging of simultaneous in-situ heating and biasing experiments in scanning/transmission electron microscopes. Microsc. Res. Tech. *79*, 239–250.

47. Koch, C. (2002). Determination of core structure periodicity and point defect density along dislocations, PhD thesis (Arizona State University).

48. Plimpton, S. (1995). Fast parallel algorithms for short-range molecular dynamics. J. Comput. Phys. *117*, 1–19.

49. Liu, H.B., and Ascencio, J.A. (2010). Structural stability and thermal transformation of Pt–Sn bimetallic nanoclusters. J. Nano Res. *12*, 131–138.

50. Rittner, J.D., and Seidman, D.N. (1996). <110> Symmetric tilt grain-boundary structures in fcc metals with low stacking-fault energies. Phys. Rev. B *54*, 6999–7015.